MASTER THESIS

Prediction of the nonlinear dynamic behaviour of a concrete slab subjected to blast load

Appendix I – Validation experiment 1

Author: L. Kraaijenbrink

Status: Final

Date: 23 August 2022

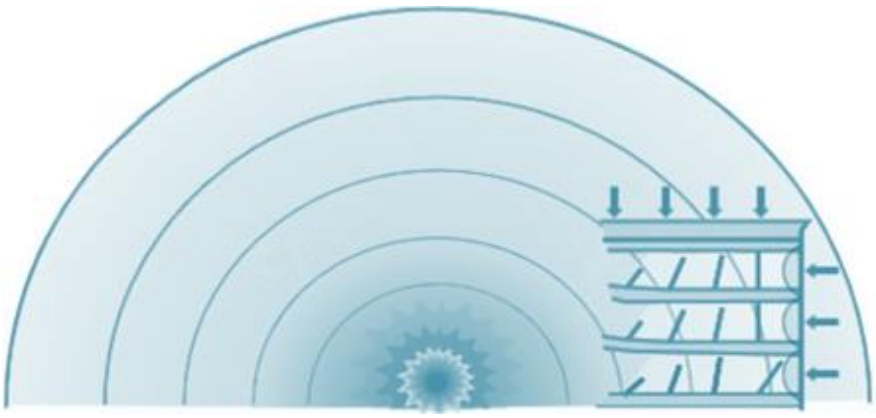

TU Delft

Royal HaskoningDHV
Enhancing Society Together

Open

HASKONINGDHV NEDERLAND B.V.

George Hintzenweg 85
3068 AX Rotterdam
Industry & Buildings
Trade register number: 56515154

+31 88 348 90 00 **T**
info@rhdhv.com **E**
royalhaskoningdhv.com **W**

Document title: Prediction of the nonlinear dynamic behaviour of a concrete slab subjected to blast load

Subtitle: Appendix I – Validation experiment 1

Status: 1.0/Final

Date: 23 August 2022

Author(s): ing. L. Kraaijenbrink

Thesis committee:		
	Prof.dr.ir. J.G. Rots	TU Delft
	Prof.dr.ir. M.A.N. Hendriks	TU Delft
	Dr.ir. K.N. van Dalen	TU Delft
	ir. P.J. Flink	Royal HaskoningDHV

Table of Contents

1 Introduction

The paper cited in this Appendix is called “Engineering and Numerical Tools for Explosion Protection of Reinforced Concrete” (Riedel et al., 2009). Numerous experiments are performed and compared with engineering tools. The experiments are conducted at the Ernst-Mach-Institut (EMI) in Germany using a shock tube. A shock tube simulates a blast load under controlled conditions. Two types of experiments are performed: one that represents a close-in detonation and one that represents far field detonations. The far field detonation is what this Appendix focusses on. The engineering tool used for the far field detonations is a pressure-impulse diagram.

The geometry of the specimen is indicated in Figure 1.1. The reinforcement has a 10 mm concrete cover. The reinforcement type BSt 500S is used, which is equivalent to B500A. The ultimate strain of this type of reinforcement may be 2.5%. In contrast to the commonly used reinforcement type B500B, BSt 500S is much less ductile.

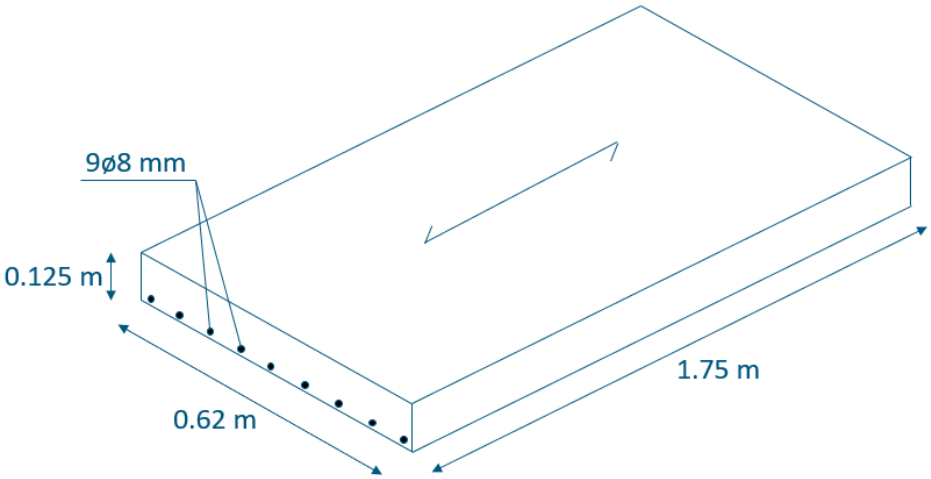

Figure 1.1: Geometry of the specimen

This Appendix presents the analysis of the experiment with the finite element method (FEM) and the finite difference method (FDM). Both methods are compared and where needed adjusted to fit the experiment. Besides the comparison between FEM and FDM and the calibration with the experiment, this document provides more insights in the analysis than Appendix II and Appendix III, such as the pressure-impulse diagram and a more in-depth explanation on the DIANA input.

The experimental results are presented in chapter 2. After that, the analysis input is addressed in chapter 3 (parameters) and chapter 4 (applied force). The finite difference model (FDM) results are presented in chapter 5 and are verified by the finite element method (FEM) analysis in chapter 6. The results are discussed in chapter 7.

2 Experiment results

The obtained results in the experiment are presented in this chapter. The goal is to recreate these results in the FEM model and FDM model.

2.1 Observations

Figure 2.1 displays the deflection curves in time of the mid-point of the beams. As Table 2.1 clarifies, the beam with the highest load is called EPR4 and the beam with the lowest load is called EPR1. EPR1 and EPR2 both remain intact, suggesting that their structural behaviour is elastic throughout the whole analysis. EPR1 is not analysed, because EPR2 will provide enough insight in the elastic behaviour of the beam. EPR4 is failing, as shown in Figure 2.2. Although EPR3 is showing cracks, it has not snapped through.

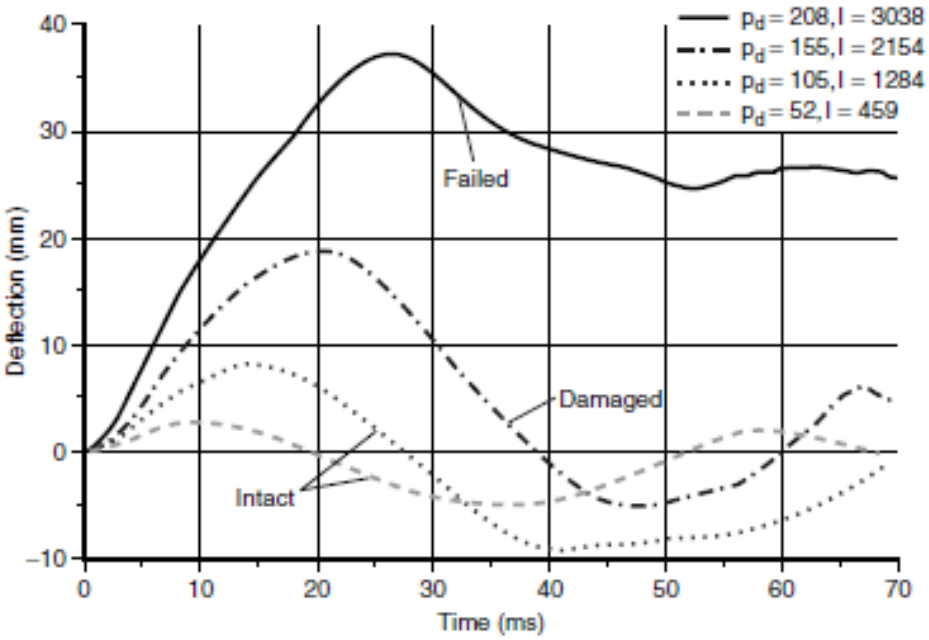

Figure 2.1: Experimental deflection-time history graph

Table 2.1: Applied impulse and pressure on the specimens

Beam	Peak pressure P_d	Impulse I	Scaled distance Z
EPR1	52	459	7.3
EPR2	105	1284	5.0
EPR3	155	2154	4.1
EPR4	208	3038	3.6

Figure 2.2: Walls after the blast. Top wall: NRC-3. Bottom wall: NRC-4

2.2 Pressure-Impulse diagram

(Riedel et al., 2009) analyses the beam with the engineering tool EMI-BEAUX. This tool creates a pressure-impulse (PI) diagram. A PI diagram is a quick method to predict damage on a structure. Figure 2.3 shows the PI-diagram that is obtained in the paper. Anything above the dotted line is the region where damage is expected.

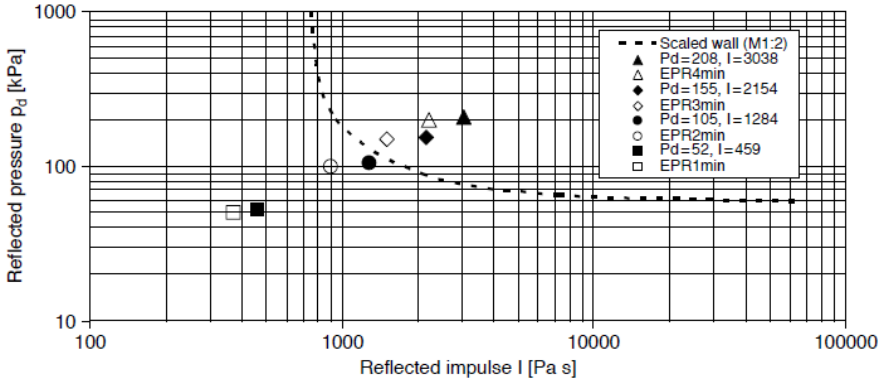

Figure 2.3: PI-diagram for the experiment parameters

The PI-diagram is shown in a log-log plot. The line has two asymptotes: an impulse asymptote and a pressure asymptote. The region where the impulse is high and the peak pressure low, is the quasi-static region. The region where the impulse is low and the peak pressure high, is the impulsive region. The region in between is called the dynamic region. The results of the experiment are located in the dynamic region, as indicated in Figure 2.4. This figure is adopted from (Abedini et al., 2018). The far field design range is almost always in the dynamic region. Near-field blast analyses are more likely to be in the impulse region.

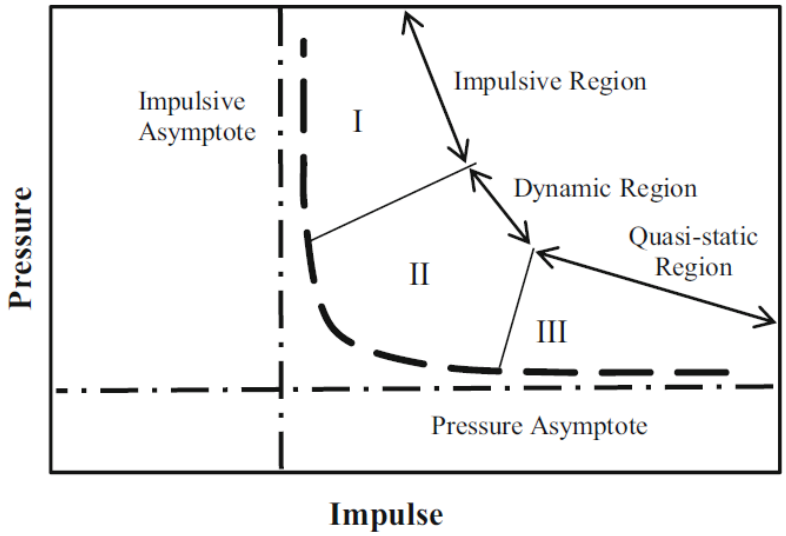

Figure 2.4: PI diagram

The PI-diagram is somewhat related to the failure mechanism. A sudden high pressure leads to more brittle and localised failure. Local failure is typical for the impulse region. Flexural failure is in most cases the governing failure mechanics for the dynamic region and quasi-static region. Figure 2.5 illustrates a few failure mechanisms for different locations in the PI-diagram. This figure is adopted from (Abedini et al., 2018).

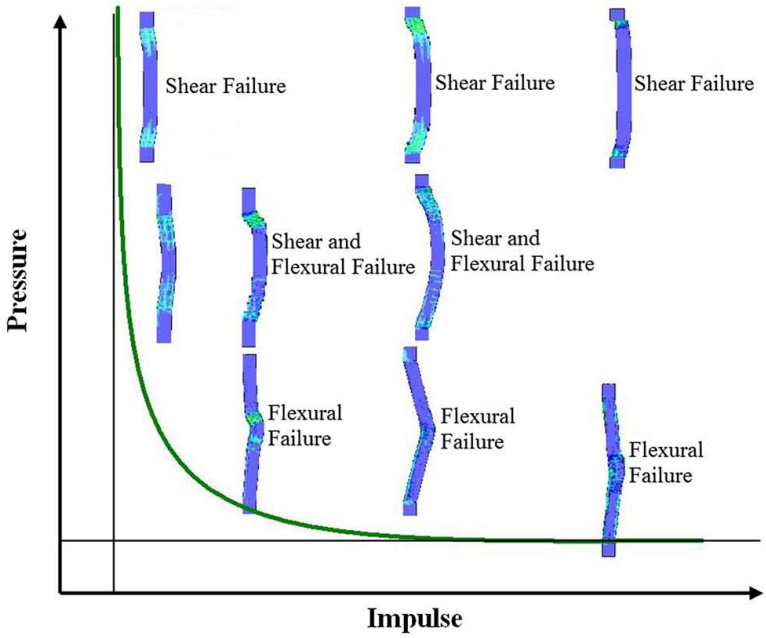

Figure 2.5: Failure mechanisms

The PI-diagram can be calculated by solving various mass-spring systems while changing the pressure and impulse each time. This approach is very time consuming. An alternative is the energy balance method. This is the most used method to derive the PI-diagram. It is based on the conservation of energy principle and works as follows:

- The impulse asymptote is obtained by assuming that the initial total energy (TE) induced by an impulse is in the form of kinetic energy (KE) (2.1). The total energy is a constant throughout the

analysis. At the point of the maximum deflection, all the energy is stored in the strain energy (SE). An expression for the impulse asymptote (2.3) is derived by equating strain energy to the kinetic energy (2.2).

$$TE = KE + SE \rightarrow TE(t=0) = KE(t=0) + 0 \tag{2.1}$$

$$KE(t=0) = SE \rightarrow \frac{I^2}{2m} = \frac{1}{2} k {u_{max}}^2 \tag{2.2}$$

$$\frac{I}{\sqrt{km}\, u_{max}} = 1 \tag{2.3}$$

- The pressure asymptote or the quasi-static asymptote is obtained assuming a constant load throughout the analysis. By equating the total work done at the point of maximum deflection to the strain energy (2.4) at the point of maximum deflection, the pressure asymptote is derived (2.5).

$$WE = SE \rightarrow F u_{max} = \frac{1}{2} k {u_{max}}^2 \tag{2.4}$$

$$\frac{F}{k u_{max}} = \frac{1}{2} \tag{2.5}$$

- The dynamic regime in the PI-diagram can be obtained by the correlation formula (2.6) suggested by (Baker et al., 1983).

$$SE = WE \tanh^2 \sqrt{KE/WE} \tag{2.6}$$

Figure 2.6 is showing two PI plots. The first one is the PI-diagram for three difference pressure functions. The previously derived asymptotes are observable. The second figure is another pressure function, typical for a roof. The pressure asymptote tends to shift up to 1.0 when the rise time to load duration ratio increases. This is because the load is applied relatively slowly, resulting in no dynamic amplification, as stated by (Krauthammer et al., 2008).

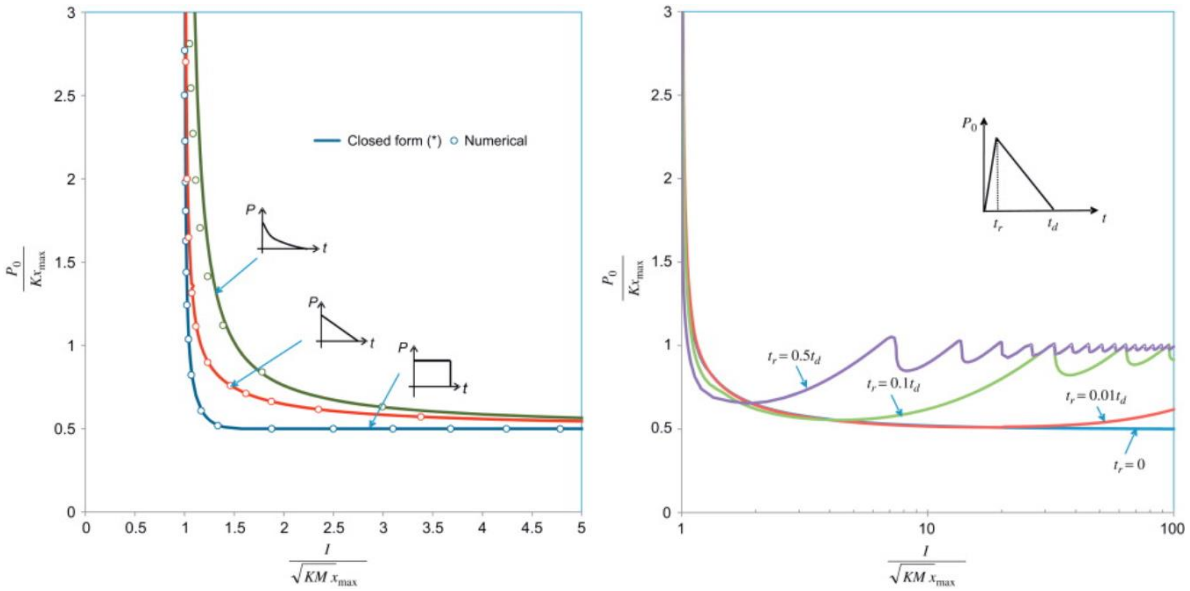

Figure 2.6: PI diagram for different loading schemes (Krauthammer et al., 2008)

3 Parameters

The parameters in the dynamic analysis are strain rate dependant. The strain rate is extracted from the analysis and can be different throughout the analysis. An average value for the strain rate is used according to (3.1) and (3.2), where t_E is the time to yield the reinforcement bars. Usually, it is enough to do one iteration: in the first analysis a reasonable strain rate is assumed. From this analysis a better strain rate can be extracted that is used in the second analysis.

$$\dot{\varepsilon}_{c,avg} = 0.002/t_E \quad (3.1)$$

$$\dot{\varepsilon}_{s,avg} = f_{dy}/(E_s t_E) \quad (3.2)$$

Table 3.1: Dynamic parameters

Parameter	Units	EPR4	EPR3	EPR2
Time to yield t_E	s	0.0065	0.0085	0.0155*
Concrete strain rate $\dot{\varepsilon}_{c,avg}$	s^{-1}	0.308	0.235	0.129
Steel strain rate $\dot{\varepsilon}_{s,avg}$	s^{-1}	0.500	0.379	0.205
DIF_c	-	1.25	1.24	1.22
DIF_t	-	1.46	1.45	1.42
DIF_E	-	1.27	1.26	1.24
DIG_{GF}	-	1.00	1.00	1.00
DIF_{GC}	-	1.25	1.24	1.22
*The reinforcement in EPR2 does not yield. An interpolation is made as follows: $\varepsilon_{sy}/\varepsilon_{s,u,max}*t_{u,max}$				

Table 3.2: Concrete properties

Parameter	Units	EPR4	EPR3	EPR2
Young's modulus (static / dynamic)	MPa	25750 / 32703	25750 / 32445	25750 / 31930
Initial Poisson's ratio	-	0	0	0
Mass density	Kg/m^3	2400	2400	2400
Tensile curve	-	Hordijk	Hordijk	Hordijk
Tensile strength (static/dynamic)	MPa	2.56 / 3.74	2.56 / 3.71	2.56 / 3.64
Fracture energy	N/m	137	137	137
Poisson's ratio reduction	-	Damage based	Damage based	Damage based
Compression curve	-	Parabolic	Parabolic	Parabolic
Compressive strength	MPa	33.00 / 41.25	33.00 / 40.92	33.00 / 40.26
Compressive fracture energy	N/m	34245 / 42906	34325 / 42464	34245 / 41779

Table 3.3: Steel reinforcement properties

Parameter	Units	EPR4	EPR3	EPR2
Young's modulus	MPa	200000	200000	200000
Yield stress (static / dynamic)	MPa	550 / 645	550 / 641	550 / 634
Ultimate engineering stress (static / dynamic)	MPa	594 / 691	594 / 688	594 / 680
Ultimate engineering strain	-	0.035	0.035	0.035

The applied concrete and reinforcement stress-strain relationships are shown in Figure 3.1 and Figure 3.2.

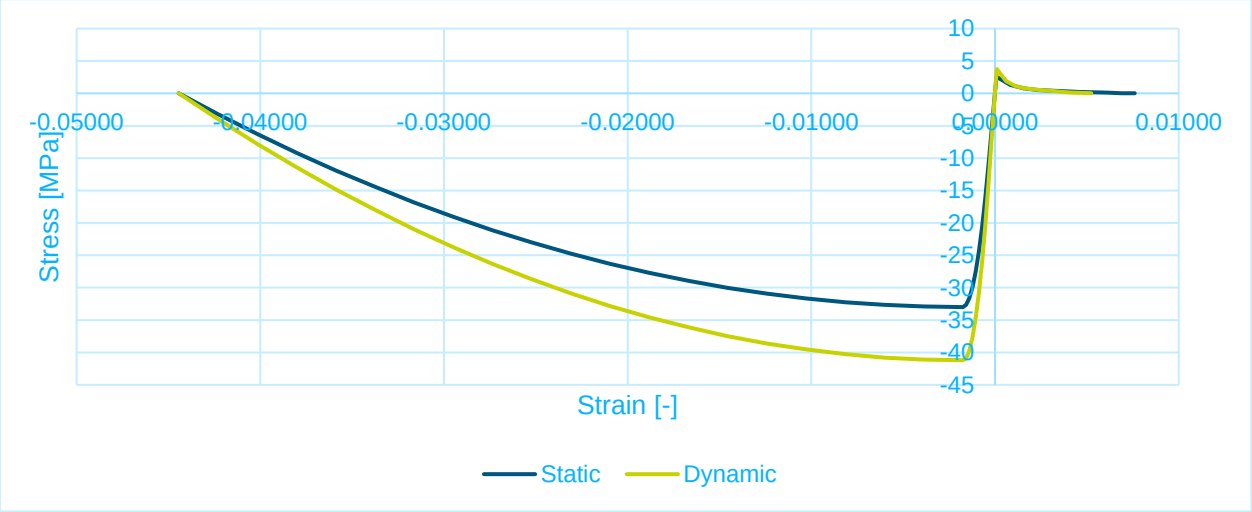

Figure 3.1: Concrete stress-strain relationship for the element length of 36.46 mm

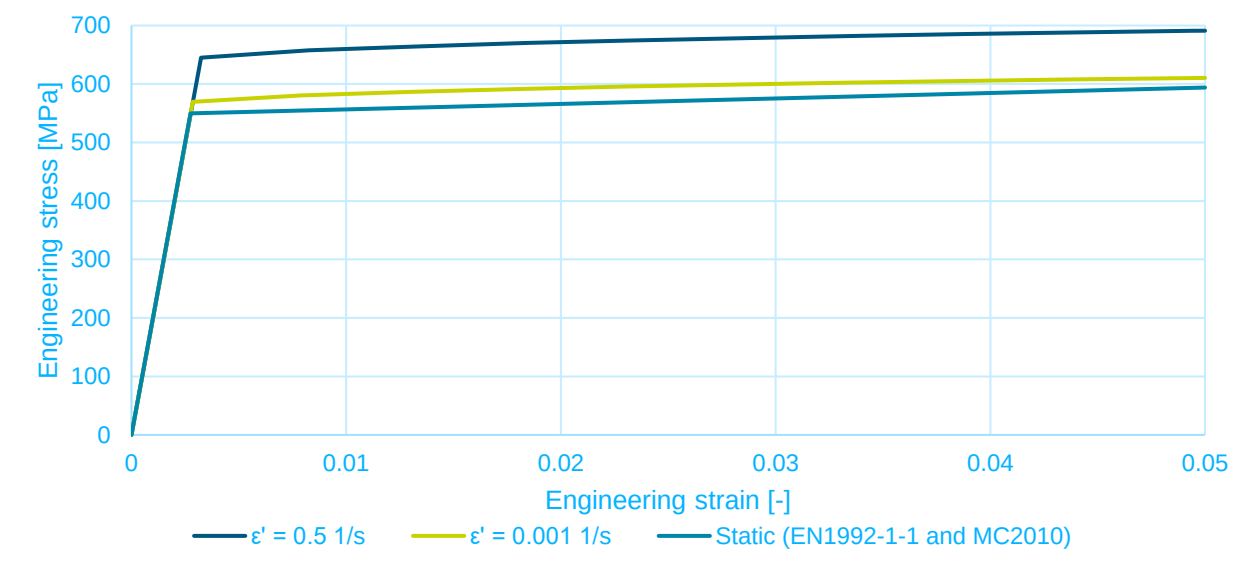

Figure 3.2: B500B stress-strain relationship

4 Applied force

The pressure function in time is not given, so an assumption must be made. The pressure function is typically exponentially shaped and is given in (4.1).

$$P_s(t) = P_{so}\left(1 - \frac{t}{t_0}\right)e^{-b\frac{t}{t_0}} \tag{4.1}$$

Where:

- P_{so} is the peak overpressure
- t_0 is the positive phase duration
- b is the decay coefficient

The impulse is calculated by integrating the pressure function over the positive phase duration. The result of this integral is given in (4.2).

$$I(t) = \int_0^t P_s(t)\,dt = \frac{P_{so}}{b^2}\left(\left((1-b)t_0 + bt\right)e^{-b\frac{t}{t_0}} + (b-1)t_0\right) \tag{4.2}$$

The impulse and peak pressure are given in Table 2.1. Two variables remain unknown: the decay coefficient b and the positive phase duration t_0. A reasonable assumption is made of those parameters. The used pressure functions are given in Figure 4.1.

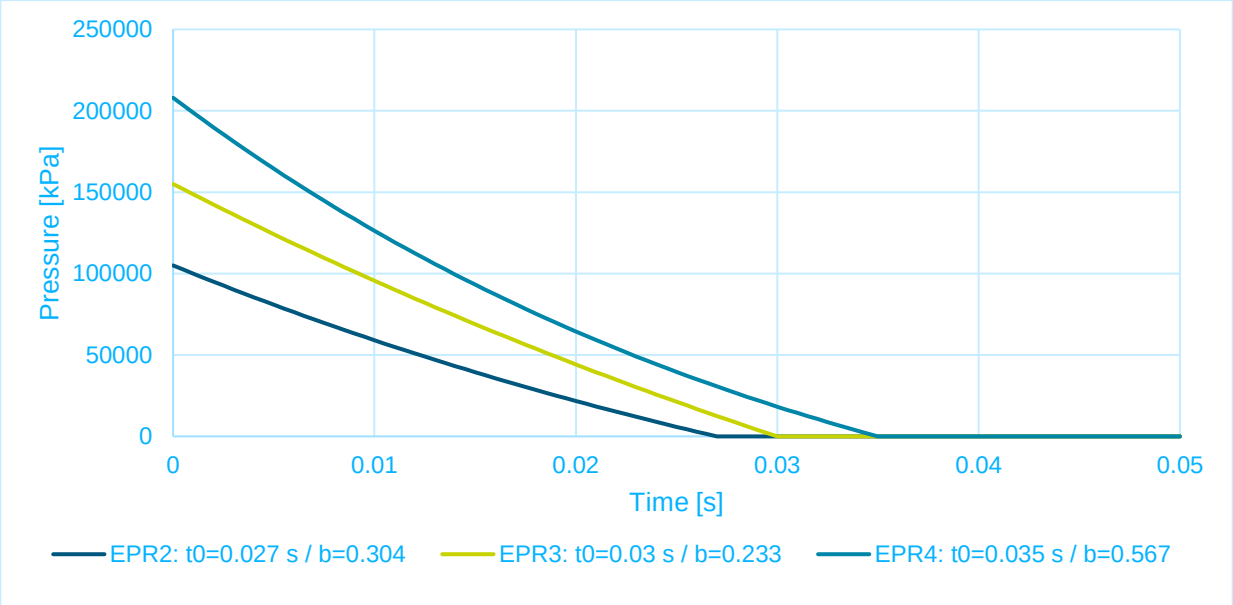

Figure 4.1: Applied pressure functions

5 FDM model

5.1 Moment curvature relationship

The M-κ graph is manually constructed and shown for the dynamic and static parameters in Figure 5.1. The M-κ graph found in the FEM analysis including dynamic parameters and with arc-length is included as a reference. There is a clear difference in the two methods. The manually constructed M-κ graph stops earlier because the concrete compressive capacity is reached. The M-κ graph in the FEM model stops when the reinforcement fails.

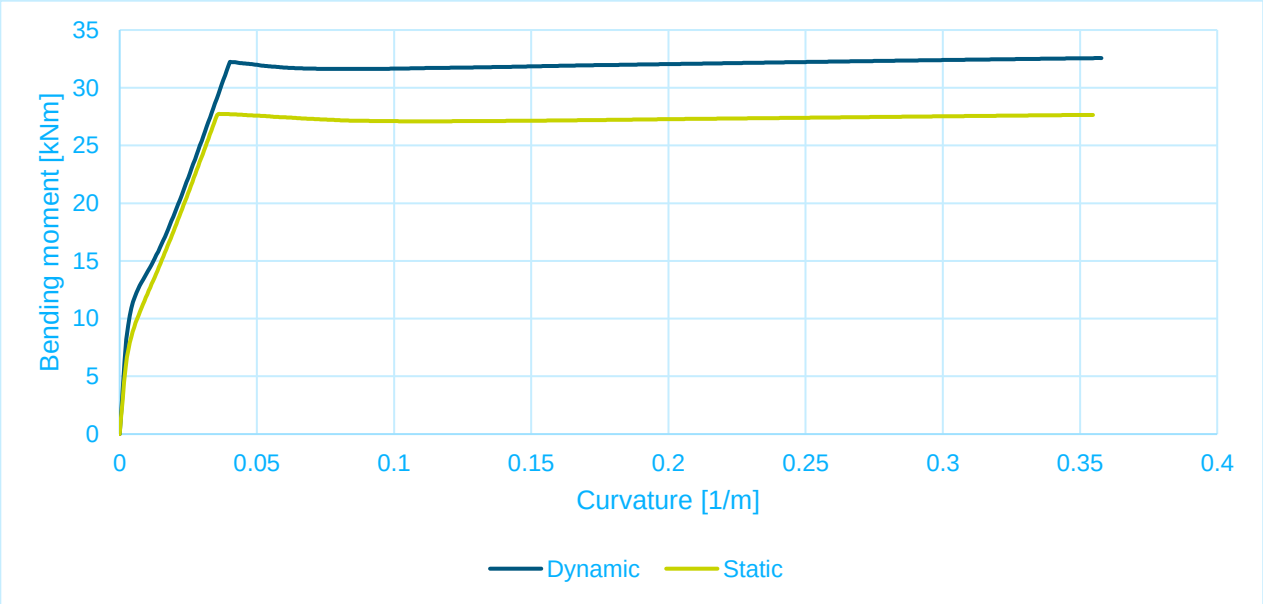

Figure 5.1: Moment-curvature graph in the FDM analysis

Table 5.1

	Units	Static	EPR4	EPR3	EPR2
Cracking bending moment	kNm	4.46	6.42	6.38	6.26
Cracking curvature	1/m	0.00159	0.00183	0.00183	0.00182
Yielding bending moment	kNm	27.64	32.24	31.87	31.64
Yielding curvature	1/m	0.0355	0.0402	0.0397	0.0395
Ultimate bending moment	kNm	27.74	32.58	32.41	32.02
Ultimate curvature	1/m	0.353	0.357	0.357	0.357

5.2 Force-displacement relationship

Since the F-u graph is derived in a force-controlled manner, The F-u graph will flatten out after reaching the force where the reinforcement starts to yield. The F-u graph stops when the end of the M-κ is reached.

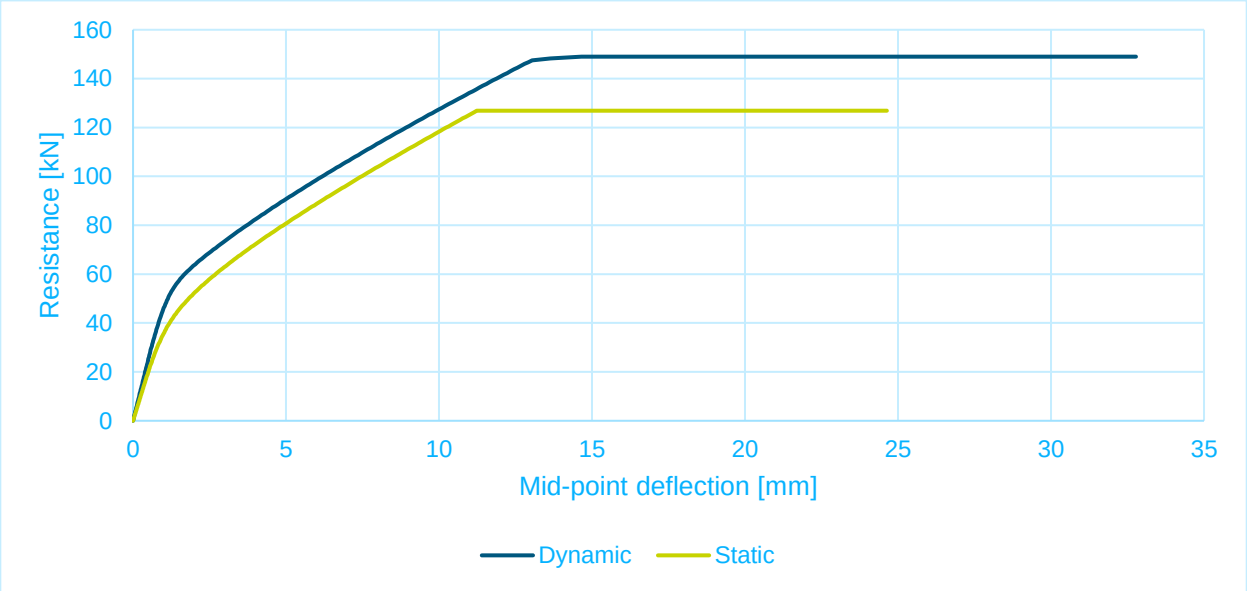

Figure 5.2: Force-displacement graph in the FDM analysis

Table 5.2

	Units	Static	EPR4	EPR3	EPR2
Cracking force	kN	20.94	29.80	29.64	29.29
Cracking deflection	mm	0.521	0.593	0.594	0.596
Yielding force	kN	126.88	147.50	146.71	144.97
Yielding deflection	mm	11.24	13.04	12.98	12.73
Ultimate force	kN	126.88	148.99	148.19	146.44
Ultimate deflection	mm	24.64	32.78	32.88	32.13

5.3 Single degree of freedom mass-spring system

Where the FEM analysis implicitly includes the participating mass and participating load, it must be manually introduced in the SDOF mass-spring system by means of the participating mass factor K_M and participating load factor K_L. The mass factor and load factor are calculated using (5.1) and (5.2), where ϕ(x) is the normalised displacement function.

$$K_M = \frac{\int_0^L m\phi(x)^2\,dx}{mL} \tag{5.1}$$

$$K_L = \frac{\int_0^L p\phi(x)\,dx}{pL} \tag{5.2}$$

For the elastic case the mass factor is 0.50 and the load factor is 0.64. For the case with a plastic hinge in the middle the mass factor and load factor will approach 0.33 and 0.5 respectively. It is highly unlikely to ever reach the lower limit since the beam would fail before the lower limit is approached.

Figure 5.3 is showing the mass factor and load factor for EPR4. The ones obtained for EPR3 and EPR2 are similar. The factors start at the upper limit, this is where the beam is still elastic. Then cracking occurs, but the reinforcement is not yielding. This causes a drop in the mass and load factor and eventually stabilises. When the plastic hinge forms, at around the mid-point deflection of 13 mm, the mass and load factor drop again and continues to drop until the beam fails.

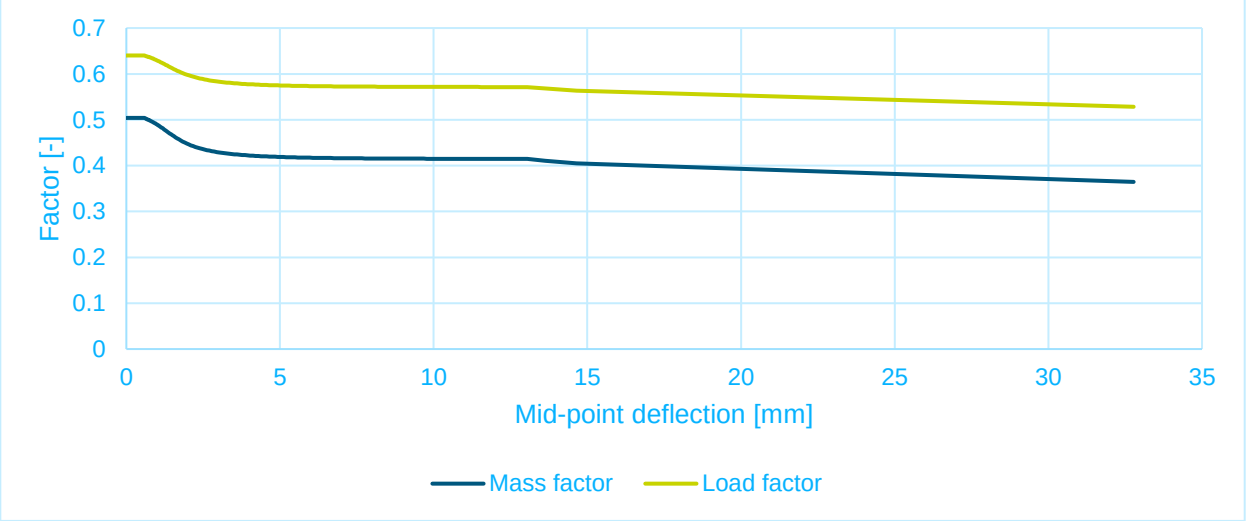

Figure 5.3: Mass factor and load factor in the FDM analysis

The mid-point deflection in time for EPR4, EPR3, and EPR2 are given in Figure 5.4. EPR4 is failing prematurely for two of the three analysed pressure functions. In the remaining analysis, the beams fail in the upwards deflection.

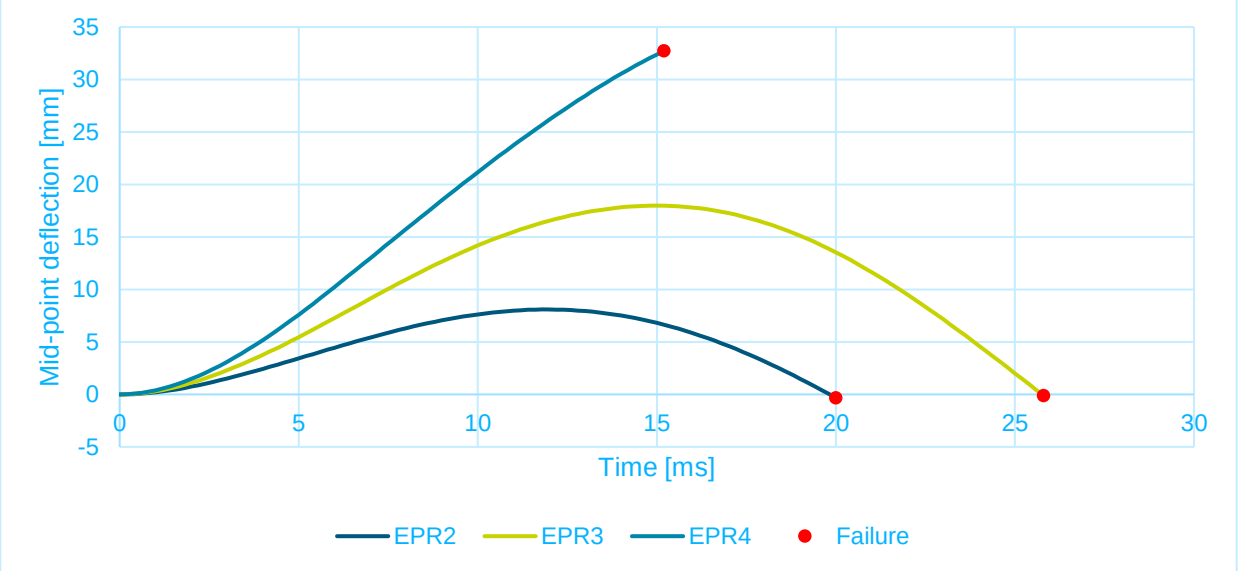

Figure 5.4: SDOF mass-spring system results

6 FEM model (DIANA)

6.1 DIANA input

In addition to the previous mentioned input, DIANA needs some additional input. This is included in this chapter.

6.1.1 Model

The specimen is modelled as a class II beam with a symmetry axis (Figure 6.1). Table 6.1 and Table 6.2 are specifying the finite elements in the model.

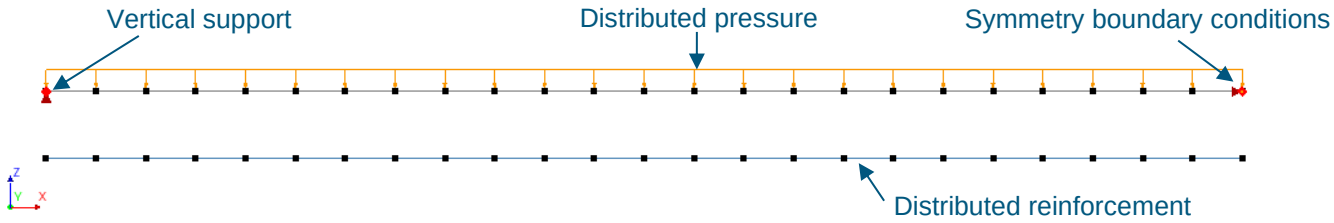

Figure 6.1: Used FEM model

Table 6.1: Used finite element type

Element type	No. of DoFs per node	Interpolation scheme	Integration scheme	Shape dimension	No. integration points over thickness
L13BE	3	Linear	2-point Gaussian	1D	19

Table 6.2: Finite element type geometry

Total no. of elements	Element length	Reinforcement eccentricity	Element height	Element width
24	36.46 mm	-48.5 mm	125 mm	620 mm

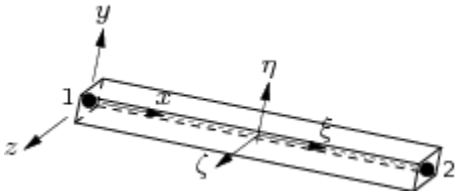

Figure 6.2: Q20SH element

6.1.2 Concrete material model

There are two main methods of modelling the cracking behaviour in concrete: discrete cracking and smeared cracking. In a discrete cracking model, the cracks are modelled as interfaces between elements. The crack location is thereby predefined. In a smeared model the cracks are spread out over an area, typically related to the element. Although a discrete cracking model should reflect the real behaviour of a structure better (when the exact crack locations are known), the smeared cracking model is the more popular choice in FEM. Regular continuum mechanics still apply in a smeared cracking model, which makes it more convenient to employ. Besides the suitability of the smeared cracking model in FEM, it is also convenient for the engineer to use. In a smeared cracking model, the crack location is undetermined on beforehand, which is most of the time the case. Secondly, a discrete cracking model requires input for the interface between elements, whereas a smeared cracking model follows the predefined constitutive relationship as the engineer is most likely used to. In DIANA this is also called the 'total strain-based crack model'. The input required for this model is included in Table 6.3.

Table 6.3: Additional required input for the total strain-based crack model in DIANA

Parameter	Units	All beams
Crack orientation	-	Rotating
Crack bandwidth	mm	36.46 (element length)
Reduction due to lateral cracking	-	Vecchio and Collins 1993
Lower bound reduction curve	-	0.4
Stress confinement model	-	None

The chosen input for the total strain-based crack model is in accordance with RTD 1016-1:2020 (Hendriks & Roosen, 2020) and Model Code 2010 (Fédération internationale du béton (fib), 2013). In short, the chosen input is based on the following:

- The constitutive relationship is evaluated perpendicular to the crack direction. The crack direction might rotate throughout the analysis. A rotating crack orientation takes this into account, while a fixed crack rotation keeps one coordinate system.
- The crack bandwidth chosen equal to the element width due to the expected crack direction (through the middle).
- The compressive strength of concrete starts to drop considerably after the occurrence of lateral cracks. The correction formula according Vecchio and Collins 1993 is used for the reduction of the concrete compressive strength due to lateral cracking
- The compressive strength of confined concrete is increased according to Selby and Vecchio. The strength is only increased when applicable, therefore it is safe to use a stress confinement model in any case.

6.1.2.1 Compressive behaviour in FEM compared with Eurocode

NEN-EN 1992-1-1 (Normcommissie 351 001 "Technische Gronslagen voor Bouwconstruties",, 2011) prescribes the compressive strain at the maximum stress of 2‰ and the ultimate compressive strain of 3.5‰. Defining prescribed strains in FEM software is inconvenient. This makes the results mesh dependant since the compressive fracture energy (area under the stress-strain curve) remains equal for any mesh size. Using an energy based concrete model for both tension and compression makes the FEM model mesh independent. Generally, this leads to a much larger ultimate strain of the discretised element.

A comparison is made between the NEN-EN 1992-1-1 concrete compressive model and the 'parabolic' curve in DIANA. The compressive fracture energy of the NEN-EN 1992-1-1 concrete compressive model

is indicated in Figure 6.3. The elastic branch is accounted for, and the curve is limited by the ultimate compressive strain. The compressive fracture energy input for the parabolic curve in DIANA is only the area below the tension softening branch, without accounting for the elastic branch (Figure 6.4). Generally, the parabolic curve goes down to 0. The compressive fracture energy is scaled by the element length h. When the element length is less than 1 m, the compressive fracture energy of the element is enlarged compared to the input value. Considering that finite elements are usually much smaller than 1 m, the ultimate compressive strain of the element is much more than 3.5‰. For large elements (> ±800 mm) the curve might be limited in a similar manner as the NEN-EN 1992-1-1 concrete compressive model.

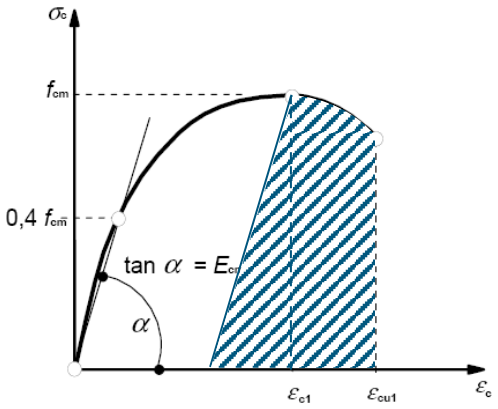

Figure 6.3: Concrete compression stress-strain relationship according to NEN-EN 1992-1-1

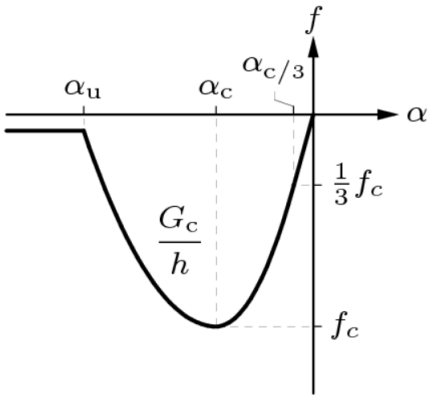

Figure 6.4: Concrete compression stress-strain relationship according to the parabolic curve

The NEN-EN 1992-1-1 concrete compressive model is formulated in (6.1), (6.2) and (6.3). The compressive fracture energy of the NEN-EN 1992-1-1 concrete compressive model can be obtained by (6.4).

$$\sigma_c = \frac{k\eta - \eta^2}{1 + (k-2)\eta} f_{cm} \tag{6.1}$$

$$\eta = \frac{\varepsilon_c}{\varepsilon_{c1}} \tag{6.2}$$

$$k = 1.05 \frac{E_{cm}\varepsilon_{c1}}{f_{cm}} \tag{6.3}$$

$$G_{c,EN1992} = \int_{\varepsilon_{c1}}^{\varepsilon_{cu1}} \sigma_c \, d\varepsilon_c + \frac{f_{cm}^2}{2E_{cm}} \tag{6.4}$$

For the static material properties mentioned in Table 3.2, the compressive fracture energy of the NEN-EN 1992-1-1 concrete compressive model is evaluated on 53966 Nm. This corresponds to the finite element length of 635 mm with the parabolic concrete compression curve in DIANA with the input compressive fracture energy of 34245 Nm (34245/0.635 = 53966).

6.1.2.2 Lateral cracking and confinement

The effects of lateral cracking and confinement are investigated by implementing them separately and observing differences in the results. In Figure 6.5, four graphs are included. Each one shows the influence of one parameter in relation to the reference model, where no additional effects are included. EPR3 is used to investigate the effects of lateral cracking and confinement.

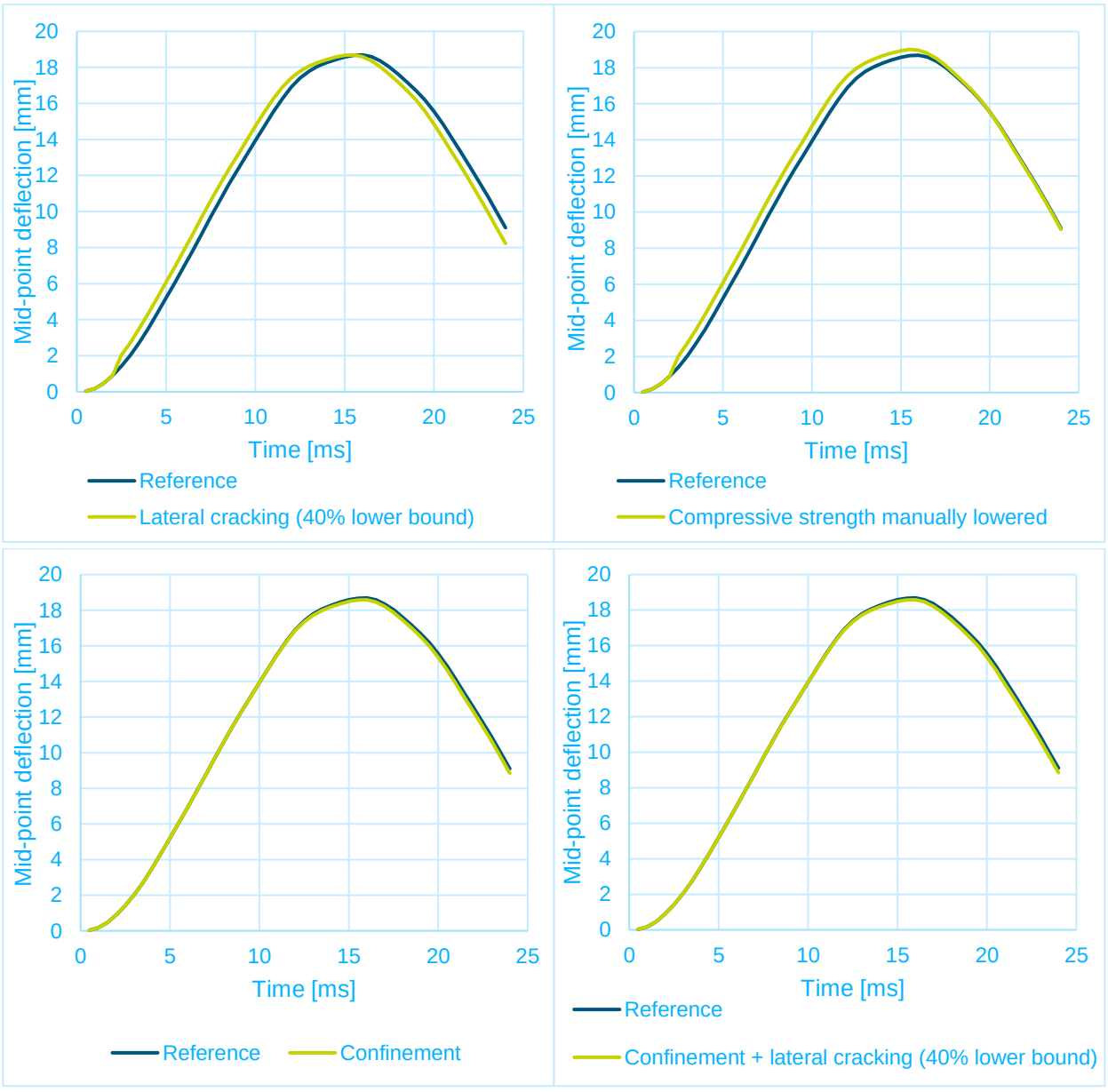

Figure 6.5: Effects of lateral cracking and confinement

At the time-step of 2 ms the deflection curve slightly jumps up for the model where the Vecchio and Collins 1993 model with lower bound of 40% is applied. This jump is also visible in the model where the compressive strength is manually lowered. This indicates that the compressive strength is indeed decreased while employing the Vecchio and Collins 1993 model. The effects of the stress confinement seem minimal, but when it is combines with the Vecchio and Collins 1993 model it seems that both effects balance each other out. Despite the lack of these effects in the FDM, it is still comparable with the FEM model because of the little influence of these effects.

6.1.3 Reinforcement steel material model

The Von Mises plasticity model is used for the reinforcement steel. The additional input for DIANA in relation to the reinforcement steel model is included in Table 6.4.

Table 6.4: Additional required input for the Von Mises plasticity reinforcement model in DIANA

Parameter	Units	All beams
Hardening hypothesis	-	Strain hardening (default)
Hardening type	-	Isotropic hardening (default)

To investigate whether DIANA uses the true stress-strain relationship or the engineering stress-strain relationship, a small test model is setup with a 1-meter-long steel bar. A prescribed deformation is applied to perform a displacement-controlled analysis. This is necessary to continue the analysis after yielding. The bar has Young's modulus of 200000 MPa and a yield strength of 500 MPa. No hardening function is used since it is not necessary to conclude whether DIANA uses the true stress-strain relationship. The Poisson's ratio is set on 0.3. An impression of the model is shown in Figure 6.6.

Figure 6.6: Used specimen for the tensile test

Three analyses are compared: one with physical nonlinearity (DIANA), one with physical and geometrical nonlinearity (DIANA) and one theoretical true stress-strain relationship. The analyses are shown in Figure 6.7. The addition of the geometrical nonlinearity in DIANA has effect. The stress gets larger than the prescribed maximum strength (yield strength) of 500 MPa. The only possible explanation is that DIANA indeed makes use of the area reduction that leads to a stress increase.
The true stress and true strain are related to the engineering strain by (6.5) and (6.6). The true stress-strain relationship deviates from the physical and geometrical nonlinear analysis in DIANA. However, in the experiment the ultimate strain is around 0.05. At this point the geometrical influence in DIANA is close to the theoretical true stress-strain.

$$\sigma_{true} = \sigma_{eng}(\varepsilon_{eng} + 1) \tag{6.5}$$

$$\varepsilon_{true} = \ln(\varepsilon_{eng} + 1) \tag{6.6}$$

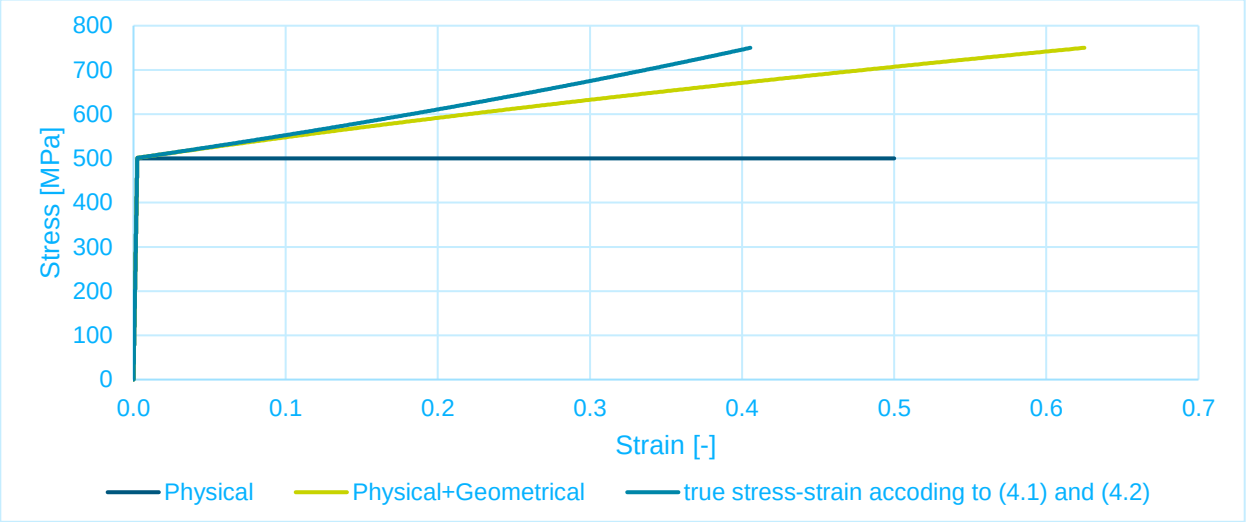

Figure 6.7: Influence of geometrical nonlinearity

6.2 Moment curvature relationship

The analysis in DIANA must be force controlled since a displacement-controlled analysis is practically impossible. In a classical force-controlled analysis, the applied force cannot decrease. However, there is the option to turn on 'arc-length control'. This is an algorithm that searches for an equilibrium path, allowing it to pass a certain limit point. The moment-curvature (M-κ) graph for the model with arc-length control is given in in Figure 6.8. The static M-κ graph is included to show the influence of the dynamic parameters compared to the static parameters.

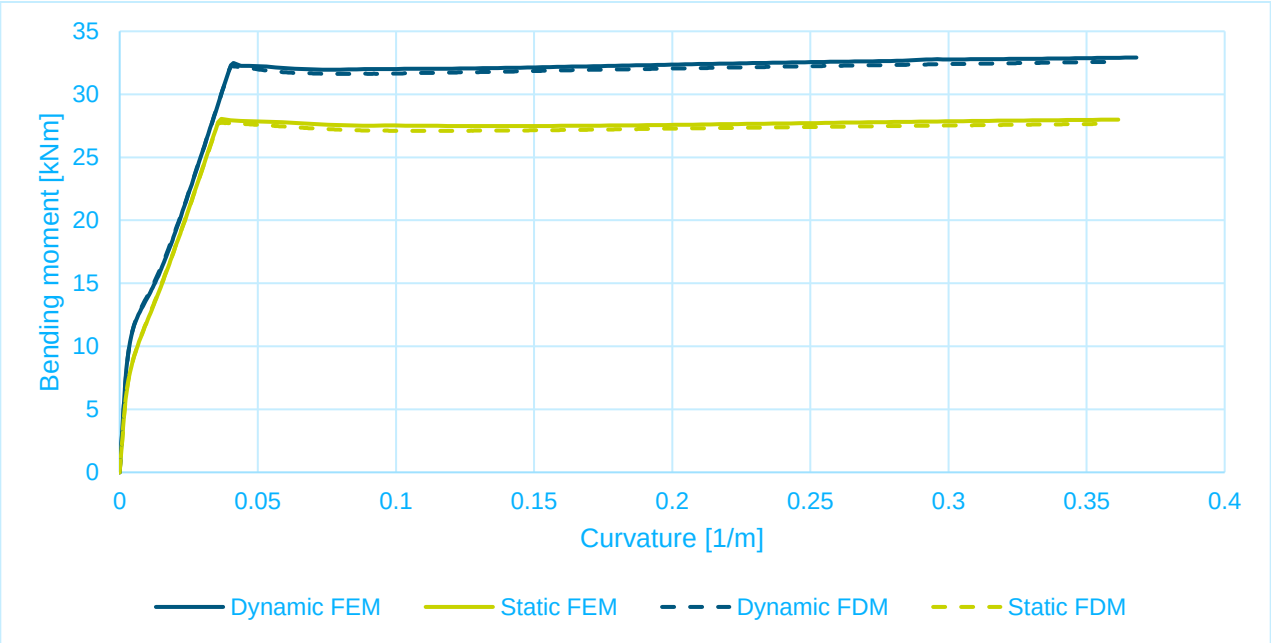

Figure 6.8: Moment-curvature relationship EPR4 (dynamic) and static

Distinct points are visible in the moment-curvature curve. The first kink indicates cracking, and the second kink indicates yielding of the reinforcement.

6.3 Force-displacement relationship

The force-displacement (F-u) graph is similar to the M-κ graph. The point of cracking and yielding of the reinforcement are well observable.

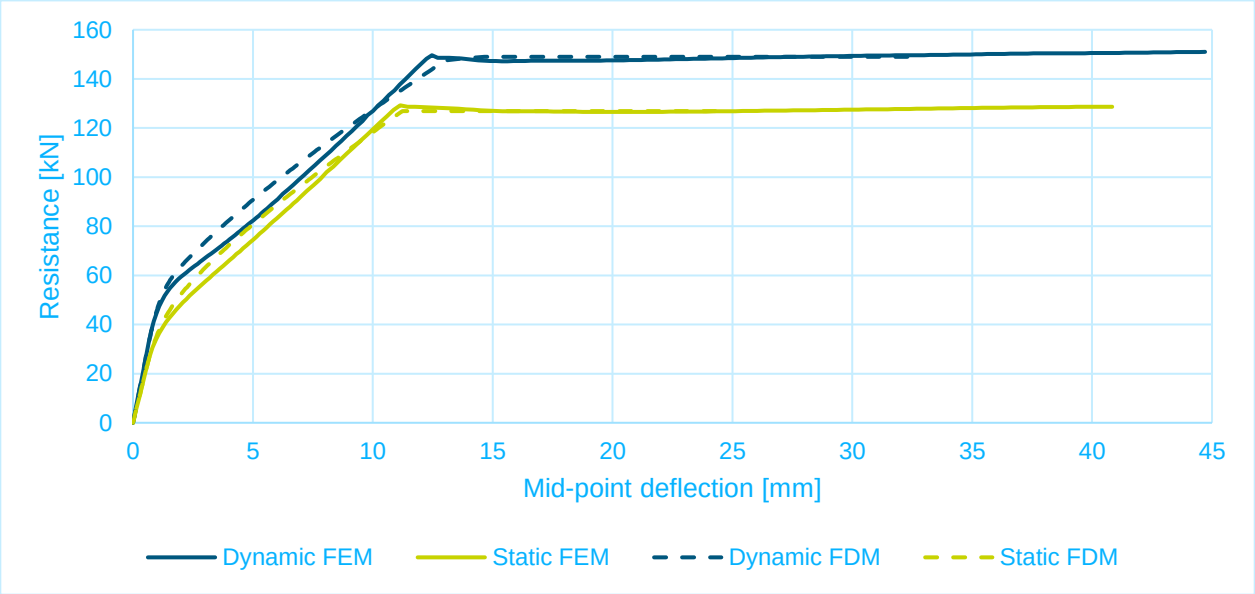

Figure 6.9: Force-displacement relationship EPR4 (dynamic) and static

6.4 Non-linear time history (NLTH) analysis

The NLTH analysis is set up as follows:

- Nonlinear effects: physical, geometrical, and transient.
- Time steps of 0.00025 seconds
- Iteration method: Secant. This is based on [NAFEMS], which states: "Newton-Raphson controlled equilibrium iteration is not always an efficient way to perform equilibrium iterations, especially if cracking is involved. The approach works well where stiffness changes gradually, for instance in plastic deformation, but not for stiffness that can change suddenly. If there is brittle behaviour, the Secant method typically provides a more stable means to reach solution convergence."
- Convergence norm: energy (tolerance: 0.001)

The mid-point deflection graphs are included in Figure 6.10. Since the reinforcement is only placed at the tension side, the inward bending motion has much lower stiffness compared to the outwards bending stiffness.

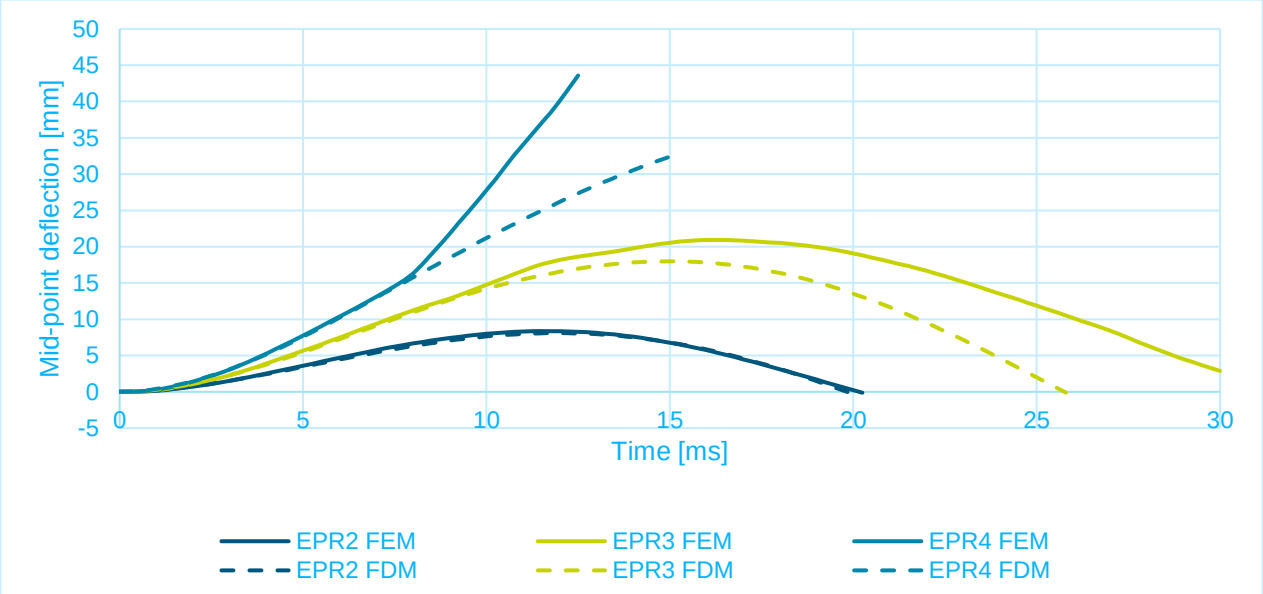

Figure 6.10: NLTH analyses with DIFs

7 Discussion

The reinforcement is only applied on one side of the beam. The inward deflection barely has any strength. Yet, the deflection curves in (Riedel et al., 2009) go way beyond the point of cracking. This is because the beam in the experiment is probably not fully restrained in the inward direction (negative deflection). Therefore, the focus in this appendix is on the first peak in the deflection curve.

Chapter 3 shows the little influence on the DIFs when the strain rate is changed within the same order of magnitude. DIFs in the far field design range should be around the values presented in this Appendix.

The constructed M-κ graph in python has good agreement with the FEM results from DIANA. The F-u graph of the FDM graph has a similar shape as the one obtained in DIANA but stops earlier. This is because the assumed plastic hinge length is shorter than the DIANA results. Considering the experimental observations, the F-u graph obtained in the FDM model is accurate. Figure 7.1 SDOF mass-spring system results with the experimental data.

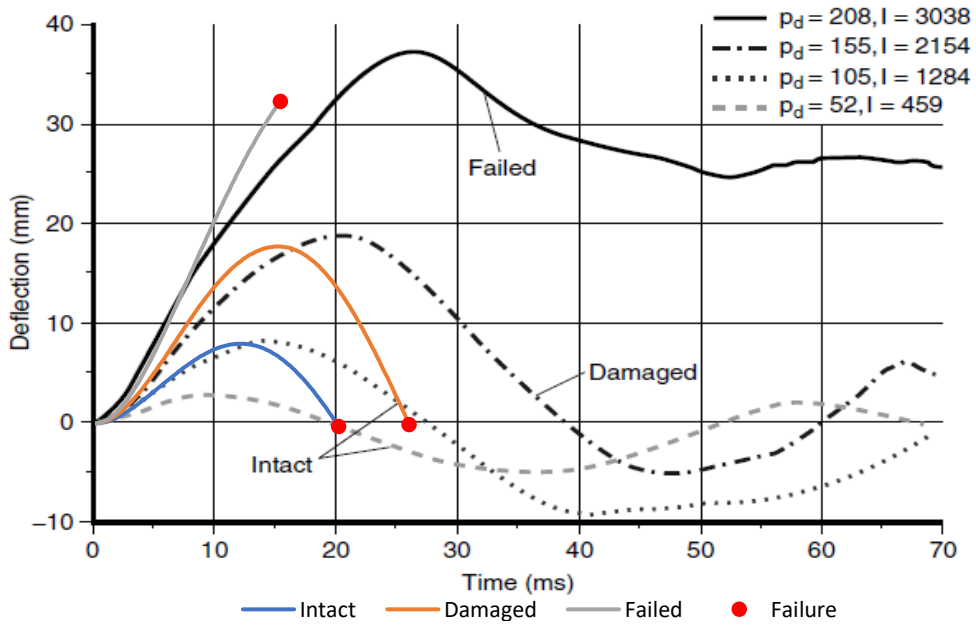

Figure 7.1: Comparison with the experiment